Chapter 9
Diagnostic Magnetic Resonance Technology

Changwook Min, Huilin Shao, David Issadore, Monty Liong, Ralph Weissleder, and Hakho Lee

Abstract For the sensitive and quantitative measurement of protein biomarkers, pathogens, and cells in clinical samples, magnetic nanoparticles (MNPs) offer unique advantages over traditional detection methods. Specifically, due to the inherently negligible magnetic background of biological material, MNPs can be used to obtain highly sensitive measurements in minimally processed samples. Our detection platform, termed diagnostic magnetic resonance (DMR), exploits MNPs to modulate the nuclear magnetic spin-spin relaxation time of water. Here, we review work done by our group to develop more effective MNP biosensors, advanced conjugational strategies to target the MNPs to molecular targets, and highly sensitive miniaturized NMR systems. We demonstrate this platform as a robust and easy-to-use system for the detection of a wide range of targets in clinical settings including whole cells, proteins, DNA/mRNA, metabolites, drugs, viruses, and bacteria.

C. Min · H. Shao · M. Liong · H. Lee (✉)
Center for Systems Biology, Massachusetts General Hospital, 185 Cambridge St, CPZN 5206, Boston, MA 02114, USA
e-mail: lee@mgh.harvard.edu

R. Weissleder
Center for Systems Biology, Massachusetts General Hospital, 185 Cambridge St, CPZN 5206, Boston, MA 02114, USA

Department of Systems Biology, Harvard Medical School, 200 Longwood Ave, Boston, MA 02115, USA

D. Issadore
Bioengineering, University of Pennsylvania, Philadelphia, PA, USA

D. Issadore and R.M. Westervelt (eds.), *Point-of-Care Diagnostics on a Chip*, Biological and Medical Physics, Biomedical Engineering,
DOI 10.1007/978-3-642-29268-2_9,

9.1 Introduction

Robust, sensitive, and easy-to-use biosensors for the detection and quantification of rare biomarkers will have significant applications in both basic research and clinical practice. If made available, these platforms could aid in understanding of fundamental biology, in accurately detecting diseases at their early stage, and in evaluating and monitoring the efficacy of therapy [1–3]. To realize such sensors, the underlying detection technology should ideally (1) enable high sensitivity and accuracy, with minimal false positives and negatives; (2) support short assay time with minimal sample processing; and (3) allow for multiplexed detection in a single parent sample [4]. Different types of sensing platforms, fulfilling some of these requirements, have been developed based on optical [5, 6], electronic [7, 8], or mass-based [9] detection. These systems, however, often require lengthy sample purification, large sample volumes, or long assay time, which can potentially limit their clinical utility and adaption.

Biosensors based on magnetic detection have recently emerged as a promising diagnostic platform. Due to the intrinsically negligible magnetic susceptibilities of biological entities, magnetic detection experiences little interference from native biological samples; even optically turbid samples will often appear transparent to magnetic fields. Biomarkers of interests, when magnetically labeled, however, can attain a high contrast against the biological background. Recent progresses in the synthesis of magnetic nanoparticles (MNPs) have further advanced the magnetic detection technology. With their size scale similar to that of biological molecules, MNPs can efficiently and abundantly bind to biological targets, amplifying analytical signals [10–13]. Various detection technologies have been developed based on this magnetic-tagging concept. These include techniques that use magnetometers, such as superconducting quantum interference device (SQUID) [14–16], magnetoresistive sensors [17–20], and Hall sensors [21], all of which directly measure the magnetic fields arising from the magnetically labeled targets.

We have recently developed a new magnetic sensing platform, diagnostic magnetic resonance (DMR) [22]. Contrary to directly measuring the magnetic moments of the labeled targets, the DMR uses nuclear magnetic resonance (NMR) as the detection mechanism. When placed in NMR magnetic fields, MNPs create local magnetic fields and change the relaxation rate of surrounding water molecules [23]. The detection offers an intrinsic signal amplification mechanism, as more than millions of water molecules can be affected by a single MNP. Moreover, since the signal is generated from the entire sample volume, the assay procedure is significantly simpler than the direct magnetic detection in which MNP-labeled targets have to be closely positioned to the sensing elements.

By optimizing MNPs and miniaturizing NMR detectors, the DMR detection sensitivities for various target types have been considerably improved over the last few years. These developments enable rapid and multiplexed detection on a wide range of targets in microliter sample volumes, including nucleic acids [24], proteins [22], drugs, bacteria [25], and tumor cells [26–28]. With the recent integration

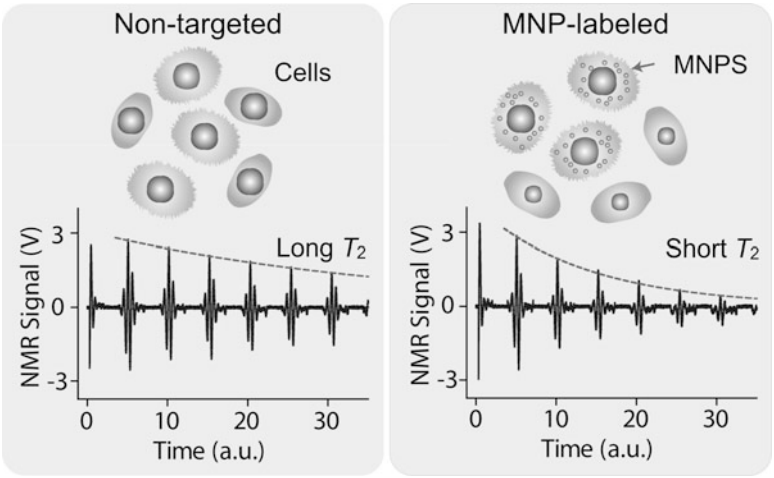

Fig. 9.1 *Principle of DMR detection*. Biological objects (e.g., cells) tagged with MNPs can accelerate the transverse relaxation of water protons. Compared to the nontagged samples, the NMR signal will decay faster in time domain, therefore providing a sensing mechanism

of bioorthogonal targeting strategies [27, 29] as well as accurate and real-time control of device temperature [23], the DMR platform has become more robust and sensitive, allowing operation in clinical settings [26]. This chapter reviews the latest development of the DMR technology, focusing on its three major components: magnetic nanoagents, miniature NMR systems, and optimized assay protocols. Specific biomedical and clinical DMR applications will also be discussed.

9.2 Principle of DMR Detection

The DMR detection of MNP-labeled cells is realized by exploiting the "T_2-shortening" effect of MNPs in NMR measurements [30]. When placed in static, polarizing magnetic fields for NMR detection, MNPs produce local dipole fields with strong spatial dependence, which efficiently destroy the coherence in the spin-spin relaxation of water protons. MNP-labeled objects consequently cause faster decay of NMR signal, or shorter transverse relaxation time T_2, than nontargeted ones (Fig. 9.1).

The capability of MNPs to induce T_2 changes is defined as transverse relaxivity (r_2) [31]. With MNPs in solution, the relaxation rate ($R_2 = 1/T_2$) can be expressed as [28]

$$R_2 = R_W + r_2 \cdot \frac{N_P}{V}, \tag{9.1}$$

where R_w is the relaxation rate of the background (usually water), V is the NMR detection volume, and N_P is the total number of MNPs in V. If each biological cell has n MNPs and the total number of cells is $N_C (= N_P/n)$, the net change of $R_2 (\Delta R_2 = R_2 - R_w)$ is given as

$$\Delta R_2 = r_2 \cdot \frac{N_P}{V} = \frac{n \cdot r_2}{V} N_c = r_2^{cell} \cdot \frac{N_C}{V}, \tag{9.2}$$

where $r_2^{cell} (= n \cdot r_2)$ is defined as the cellular relaxivity (transverse relaxivity per given cell concentration). Note that r_2^{cell} is indicative of the abundance of relevant surface biomarkers. NMR thus can be used effectively for molecular profiling of target cells [27,28]. Equation 9.2 provides valuable insights into how to increase the sensitivity and specificity of NMR-based sensors:

- *MNPs with high r_2 relaxivity*. Pronounced R_2 changes will occur when cells are labeled with MNPs of high r_2 relaxivity [23]. Because r_2 is proportional to the magnetic moment (μ_p) of particles [32,33], making magnetically stronger MNPs will benefit the measurements.
- *Maximal MNP labeling on cell.* The R_2 changes are also directly proportional to the number of MNPs loaded onto cells. In addition to increasing the r_2 potency of individual MNPs, it is equivalently important to establish a labeling protocol to maximize and/or amplify MNP loading on cells.
- *Miniaturized NMR probes.* Higher sensitivity can be achieved on the device level by decreasing the NMR detection volume (V). This approach can effectively increase the analyte concentration (N_C/V), leading to large ΔR_2. Furthermore, smaller NMR probes assume higher SNR (signal-to-noise) ratio due to the increased sample filling factor. It can be shown that the sensitivity of NMR coils (with a typical dimension of d) scales as $d^{-1/2}$ [34].

These recognitions motivated us to explore three major activities in DMR development: synthesis of new MNPs, optimization of such MNPs for cellular labeling, and miniaturization of NMR systems. The following sections will describe these accomplishments.

9.3 New Magnetic Nanoparticles

We have developed many different types of MNPs (Table 9.1) and engineered the particle size and composition to enhance the transverse relaxivity. According to the outer-sphere model of transverse relaxation, the r_2 value of an MNP is proportional to $\tau_d \cdot M^2$, where τ_d is the residence time of water molecules around the particle and M is the particle magnetization [35]. The efforts to enhance r_2 were thus focused on synthesizing larger MNPs using magnetically stronger material. We herein introduce two types of such particles: metal-doped ferrite and iron (Fe)-based MNPs.

Table 9.1 MNPs developed for DMR applications

MNP core material		Core size (nm)	Per nanoparticle	
			Magnetic moments ($\times 10^{-15}$ emu)	r_2 relaxivity ($\times 10^{-15}$ $s^{-1} \cdot L^{-1}$)
Ferrite	MION	3	0.003	0.05
	CLIO	7	0.03	0.92
	PION	11	0.1	12
	Fe_3O_4	16	0.7	23
Doped ferrite	$CoFe_2O_4$	16	0.7	31
	$MnFe_2O_4$	16	0.8	60
Fe-core particles	Fe@FeO	16	1.1	41
	$Fe@Fe_3O_4$	16	1.5	50
	$Fe@MnFe_2O_4$	**16**	**1.6**	**68**

9.3.1 Ferrite-Based MNPs

With their excellent stability and biocompatibility, cross-linked iron oxide (CLIO) nanoparticles have been widely used for DMR applications [22,36]. CLIO nanoparticles contain a superparamagnetic iron oxide core (3–5-nm monocrystalline iron oxide) composed of ferrimagnetic magnetite (Fe_3O_4) and/or maghemite (γFe_2O_3). The metallic core is encased with biocompatible dextran, which is cross-linked and functionalized with primary amine. Amine-terminated CLIO nanoparticles have an average hydrodynamic diameter of 38 nm, and about 60 amine groups are available for bioconjugation per nanoparticle. The r_2 of CLIOs is $\sim 50\ s^{-1} mM^{-1}$ [Fe] [24,37] as measured at 40°C and at the external field of $B_0 = 0.5$ T.

Two main strategies have been employed to further improve the magnetization of ferrite nanoparticles and thereby the r_2 relaxivity: magnetic doping and nanoparticle sizing. Magnetic doping with ferromagnetic elements such as manganese (Mn), cobalt (Co), or nickel (Ni) has been known to modulate the overall magnetization of MNPs [38,39]. Among these doped ferrite MNPs, $MnFe_2O_4$ nanoparticles have the highest magnetization, as Mn^{2+} ions have the highest spin quantum number (5/2). Moreover, larger nanoparticles are also known to have increasing magnetization [40]. Spin canting, a feature that decreases the overall magnetic moment of small nanoparticle due to tilted surface spins, can be reduced in bigger nanoparticles to increase the overall magnetization. Concurrently, larger particle size further enhances the particle r_2 by increasing τ_d.

We employed both magnetic doping and sizing strategies to produce $MnFe_2O_4$ nanoparticles with superior r_2 relaxivity [28]. These particles were synthesized in the organic phase by reacting iron (III) acetylacetonate [$Fe(acac)_3$], manganese (II) acetylacetonate [$Mn(acac)_2$], and 1,2-hexadecanediol at elevated temperature (300°C). Through a seed-mediated growth approach, the particle size was stepwise increased from 10 nm to 12, 16, or 22 nm. $MnFe_2O_4$ nanoparticles with diameter $\leq$16 nm were found to be highly monodisperse and superparamagnetic at 300 K

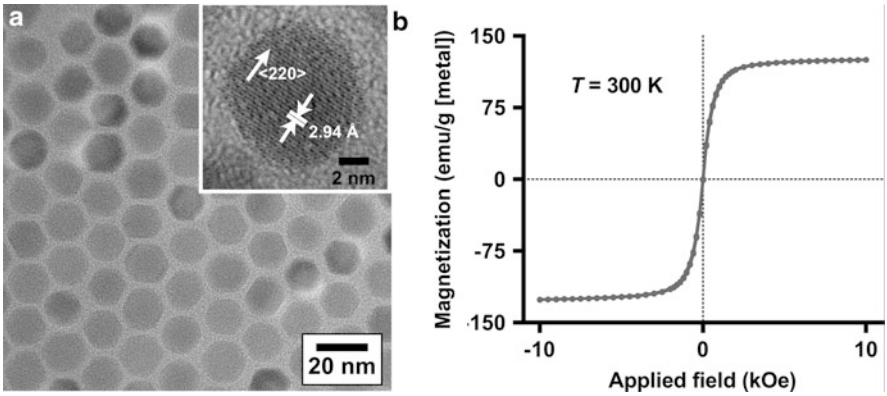

Fig. 9.2 *Mn-doped ferrite for DMR detection.* (**a**) Transmission electron microscope (TEM) images of $MnFe_2O_4$ MNPs prepared in our laboratory. The particles have a narrow size distribution and consisted of a single crystal (*insets*). (**b**) The particles in (**a**) showed superparamagnetic behavior at room temperature (Adopted from [28]. Copyright 2009 National Academy of Sciences, USA)

(Fig. 9.2). Because of their larger magnetic core, these $MnFe_2O_4$ nanoparticles assumed high relaxivities with r_2 values approaching 420 $s^{-1}.mM^{-1}$[metal] (equal to $6 \times 10^{-14} L \cdot s^{-1}$ per particle), more than eight times greater than CLIO nanoparticles in metal basis (50 $s^{-1}mM^{-1}$[metal] or $7 \times 10^{-16} L\, s^{-1}$ per particle) [28].

9.3.2 Fe-Core MNPs

Ferromagnetic metals, instead of their oxides, have been suggested as an ideal constituent of MNPs for their superior magnetization. However, while Fe-core MNPs can achieve high r_2 relaxivities [41], these monometallic MNPs are extremely reactive and require protective layers to prevent rapid oxidation.

Recently, a unique 16-nm Fe-core/ferrite-shell MNP (Fe@ferrite) has been developed for DMR applications (Fig. 9.3) [42]. The particle consists of an elemental iron core (not iron oxide) and a protecting oxide shell. A novel synthetic route was established, as summarized below, that allows for the preparation of large yet monodisperse Fe MNPs and the growth of protective ferrite shells around existing Fe MNPs (Fig. 9.3a).

- *Larger Fe cores.* Fe MNPs were formed by thermally decomposing metal complexes [$Fe(CO)_5$] in the presence of surfactant (oleylamine) under air-free condition. By increasing the reaction temperature during Fe MNP synthesis, the particle size could be proportionally increased [42]. The phenomenon can be attributed to the higher reactivity of Fe ions at elevated temperatures during particle formation [43]. Applying this approach, Fe MNPs with diameters up to 18 nm could be prepared while maintaining the relative size variations <5%.

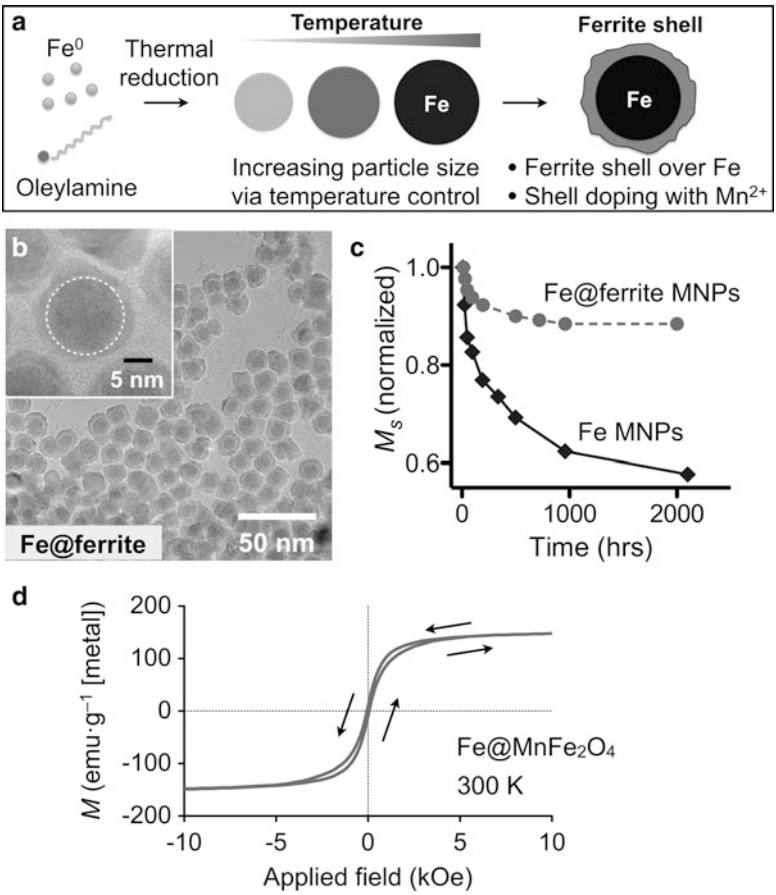

Fig. 9.3 *Fe@ferrite MNPs.* (**a**) New synthetic route. The size of the Fe core is increased by elevating the reaction temperature. The core is then overcoated with a ferrite shell. To further enhance the particle magnetization, the shell is metal doped. (**b**) TEM image of Fe@ferrite MNPs. Fe MNPs (*dotted circles*) were preserved during the coating process. (**c**) Fe@ferrite MNPs showed stable magnetic properties over time with small changes (<10 %) in saturation magnetization (M_s). (**d**) The field-dependent magnetization (M) of Fe@MFe_2O_4 MNPs at 300 K showed an unusual feature: negligible remanent moments but the presence of hysteresis (Adopted from [42]. Copyright 2011 John Wiley and Sons, Inc.)

- *Ferrite-shell overcoat.* Native Fe MNPs undergo rapid oxidation, which necessitates the presence of protective shells. To prepare such shells, we carried out the reaction for ferrite synthesis in the presence of as-prepared Fe MNPs, based on the hypothesis that Fe MNPs could serve as nucleation sites for ferrite formation. Indeed, the resulting particles (Fe@ferrite, Fig. 9.3b) had Fe cores whose sizes were similar to that of the initial Fe MNPs (dashed circles in Fig. 9.3b). Importantly, Fe@ferrite MNPs maintained their shape and magnetic properties over time (Fig. 9.3c), verifying the sturdy protection against oxidation

by the shell. Note that we further enhanced the overall magnetic moment and r_2 relaxivity by doping the ferrite with Mn^{2+} during the shell formation (Fe@$MnFe_2O_4$ MNPs).

The Fe@ferrite MNPs assumed higher saturation magnetization (796 kA m^{-1}) and r_2 (7×10^{-14} $L\,s^{-1}$ per particle, 430 $s^{-1}mM^{-1}$[metal]) than similarly sized ferrite MNPs, primarily due to the large Fe cores. It is noteworthy that the Fe core is in a thermally stable ferromagnetic state with nonzero coercivity. The ferrite shell, which is superparamagnetic, however, effectively reduces the overall coercivity of particles by leading the magnetization processes at small external magnetic fields [42]. The resultant Fe@ferrite MNPs thus displayed a unique magnetic feature, namely, the presence of hysteresis with negligible coercivity (Fig. 9.3d). This property is crucial in preventing interparticle aggregations from magnetic interactions. When applied for DMR assays, these Fe@ferrite MNPs achieved superior performance, capable of detecting picomolar avidin and single cancer cells in whole blood samples.

9.4 Optimizing MNPs for DMR Applications

In addition to the above-mentioned strategies to improve nanoparticle relaxivities through inorganic chemistry, postsynthesis modifications such as better particle surface chemistry and new labeling approaches have also been developed for DMR applications. These novel postsynthesis modifications not only improve the detection sensitivities but also simplify the targeting assays, making the DMR platform easily applicable to detect a wide range of biological entities and translatable for effective clinical utility.

9.4.1 Biocompatible Coating on Hydrophobic MNPs

Most MNPs, synthesized via the thermal decomposition method, are suspended in nonpolar solvents and coated with hydrophobic surfactant. For biological applications, these particles should be transferred into aqueous phase. We have traditionally used a small bifunctional molecule DMSA (meso-2,3-dimercaptosuccinic acid) to replace hydrophobic capping layers (e.g., oleic acid or oleylamine) on MNP surfaces [44,45]. The resulting particles, however, displayed short-term stability (<3 month), gradually precipitating out in physiological buffers [44].

Overcoming the issue, we have established a new, polymer-based surface coating that can render MNPs hydrophilic with superb stability under varying pH and ionic strength (Fig. 9.4a) [46]. As a coating substrate, we selected polyvinyl alcohol (PVA) since the material is synthetic, inexpensive, hydrophilic, and biodegradable [47–49]. The polymer was further modified into carboxymethyl polyvinyl alcohol (CMPVA); we hypothesized that multidentate carboxylic (-COOH) groups would

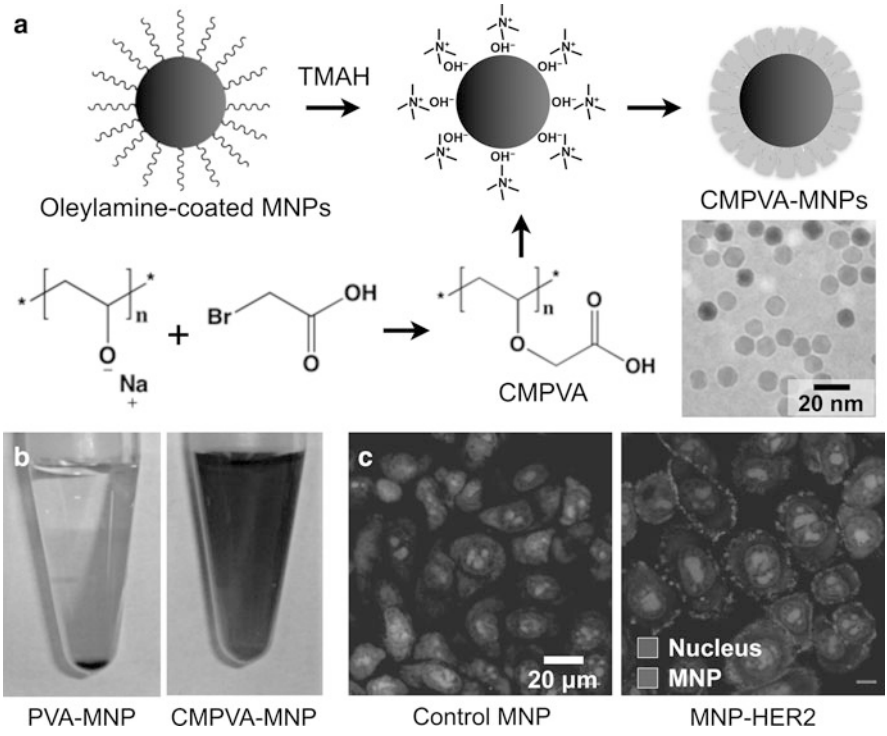

Fig. 9.4 *Highly stable polymer coating on MNPs*. (**a**) Hydrophobic layers on MNPs were first replaced with TMAH (tetramethylammonium hydroxide) and then further coated with carboxymethyl polyvinyl alcohol (CMPVA). TEM confirms that the particles are well dispersed in water after the CMPVA coating. (**b**) The presence of carboxylic acids on polyvinyl alcohol (PVA) is crucial to the stability of the coating; PVA-coated MNPs aggregated in aqueous solutions. (**c**) Cancer cells (SkBr3) were labeled with fluorescent CMPVA-MNPs by targeting HER2/neu surface receptors. CMPVA coating displayed remarkably low nonspecific binding to the cells (Reproduced from [46]. Copyright 2010 John Wiley and Sons, Inc.)

allow CMPVA to strongly bind to the metal oxide surface. Indeed, when hydrophobic $MnFe_2O_4$ MNPs were coated with CMPVA, the particles showed excellent, long-term solubility (>12 months) in aqueous buffers, whereas PVA-coated particles precipitated spontaneously (Fig. 9.4b). CMPVA coating also provided free amine ($-NH_2$) groups for bioconjugation.

When tested for cellular labeling, the CMPVA coating exhibited extremely low nonspecific binding. Figure 9.4c shows an example of cellular labeling with CMPVA-MNPs. Cancer cells (SkBr3) were first labeled with biotinylated anti-HER2/*neu* monoclonal antibodies, followed by an incubation with neutravidin-modified, fluorescent CMPVA-MNPs. Control samples were prepared in the same way but without antibody injection. Strong fluorescence signal could be visualized on the surface of targeted cells, whereas the signal from control samples was

negligible. This obvious difference between the control and positively labeled samples is highly important for DMR assay in reducing false positives in biosensing.

9.4.2 New Labeling Method for High MNP Loading

Besides improving the physical properties of MNPs, equally important for the DMR assay is to develop an efficient method for MNP labeling on target cells. A conventional way is to use MNPs preconjugated with target-specific affinity ligands [22], which often requires extensive optimization of the affinity ligands and the conjugation method for each new target.

We have developed a new targeting strategy, BOND (bioorthogonal nanoparticle detection), that is modular and broadly applicable and can amplify MNP binding to biological objects [27]. The BOND is based on [4 + 2] Diels-Alder cycloaddition, especially between tetrazine (Tz) and *trans*-cyclooctene (TCO; Fig. 9.5a) [50]. The reaction is fast and irreversible (covalent) and can be performed at room temperature without using any catalyst (copper). We have adapted the chemistry for MNP labeling of cells (Fig. 9.5b), wherein cells are pretargeted with TCO-modified antibodies and subsequently incubated with Tz-loaded MNPs (Tz-MNPs). Multiple TCO tags (usually ∼20) could be incorporated onto an antibody, and such modified antibodies were found to maintain their affinity. Consequently, the antibodies functioned as a scaffold to promote multiple attachments of Tz-MNPs. Indeed, flow cytometry measurements showed that the BOND yielded ∼15-fold improvement in MNP loading on cells, compared to labeling with antibody-MNP direct conjugates (Fig. 9.5c). The trend was further confirmed in NMR-based cell detection (Fig. 9.5d); the BOND method yielded more pronounced T_2 changes and improved the cellular detection limit.

BOND has been successfully adapted for DMR molecular profiling of experimental cellular samples [27] and clinical fine-needle aspirate samples [26]. Recently, the BOND technology was further generalized by developing newer two-step detection schemes based on complementary oligonucleotide approaches [29], alternative cycloaddition chemistries [51], and cyclodextrin/adamantine supramolecular interactions [52].

9.5 Miniaturized NMR System

The development of miniaturized nuclear magnetic resonance (μNMR) systems [22] represents a key milestone in sensitive detection in DMR. Device miniaturization brings several distinctive advantages for sensitive detection and clinical translation. First, it provides a promising way to improve the detection sensitivity. Smaller NMR systems reduce the detection volume, which in turn effectively increases the concentration of MNP-targeted cells for large R_2 changes (Eq. 9.3)

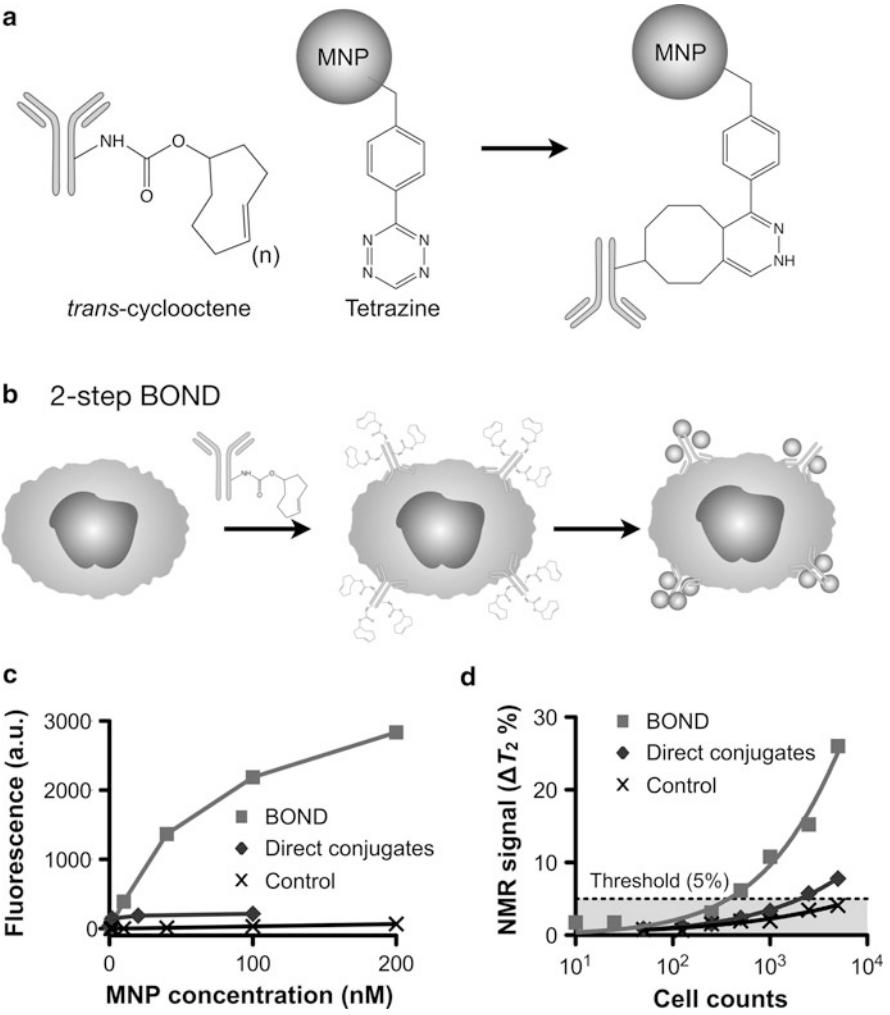

Fig. 9.5 *Bioorthogonal nanoparticle detection (BOND).* (**a**) The method is based on the Diels-Alder cycloaddition between trans-cyclooctene (TCO) and tetrazine (Tz). (**b**) Cells are prelabeled with TCO antibodies and targeted with Tz-MNPs. The antibody provides sites for mutliple MNP couplings. (**c**, **d**) Compared to the direct targeting with MNP-antibody conjugates, BOND method enabled higher MNP loading on target cells as confirmed by fluorescent (**c**) and μNMR (**d**) measurements (Reproduced from [27]. Copyright 2010 Nature Publishing Group)

Second, miniaturized NMR probes (coils) produce much stronger radio-frequency (RF) magnetic fields per unit current, leading to higher signal-to-noise per unit sample volume [53]. Third, with smaller RF coils, the requirement for spatial homogeneity of static magnetic fields becomes less stringent, making it possible to use small, portable magnets [22]. The entire measurement system can be realized as a portable device for point-of-care operations.

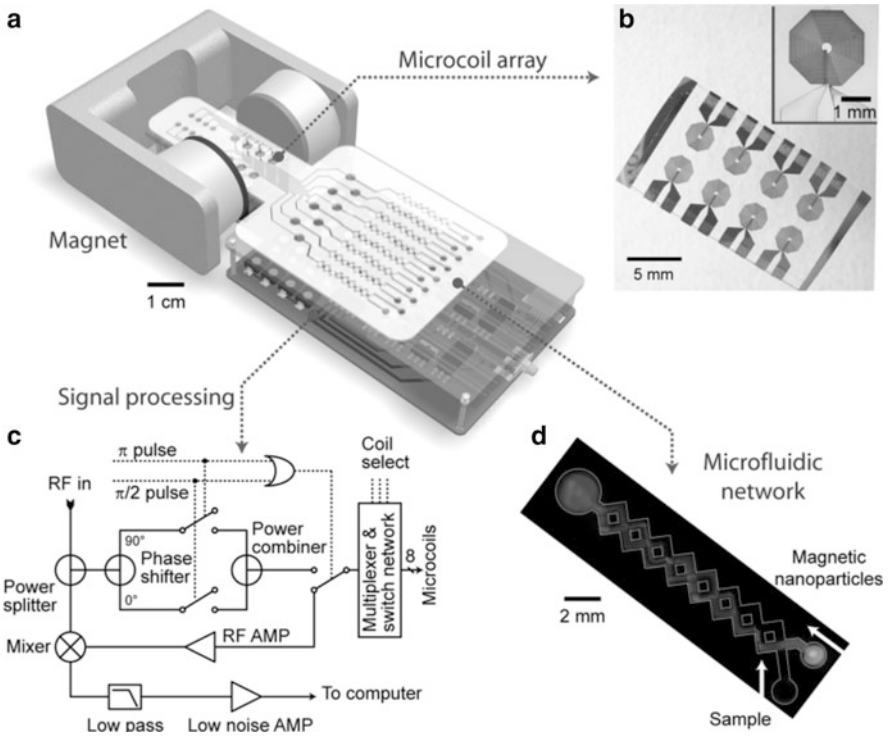

Fig. 9.6 *Schematic of microNMR system*. (**a**) The system consists of an array of microcoils for NMR measurements, microfluidic networks for sample handling and mixing, embedded NMR electronics, and a permanent magnet for polarizing magnetic field generation. The whole setup can be packaged as a handheld device for portable operation. (**b**) Micrograph of a microcoil array. The microcoil (*inset*) generates RF magnetic fields to excite samples and receives the resulting NMR signal. (**c**) Schematic of the NMR electronics. The circuit is designed to perform T_1 and T_2 measurements via inversion recovery and CPMG (Carr-Purcell-Meiboom-Gill) pulse sequences, respectively. (**d**) Example of a microfluidic network for effective mixing between magnetic nanoparticles and the samples (Reproduced from [22]. Copyright 2008 Nature Publishing Group)

9.5.1 System Concept

NMR-based cell detection has been previously performed on benchtop relaxometers (e.g., minispec, Bruker) [36,54–56]. The systems are equipped with permanent, low-field (<1 T) magnets for field generation, which simplifies operation and housing of the equipments; however, the main drawbacks of the benchtop system include the use of relatively large sample volumes (~100 μL) and the lack of capability for parallel measurements.

Overcoming these limits, the first μNMR prototype was designed and tested for the feasibility of miniaturization. Figure 9.6 shows the main features of the μNMR

system: planar microcoils, microfluidic networks, onboard NMR spectrometer, and a portable magnet. The microcoils are used for NMR detection and are arranged in an array format for parallel measurements. The microfluidic networks facilitate the handling and distribution of small volumes of samples. A small, portable magnet (NdFeB, $B_0 = 0.5\,\mathrm{T}$) was employed to generate NMR field. The system measured the T_1 relaxation time using inversion recovery pulse sequences; for T_2 measurements, Carr-Purcell-Meiboom-Gill (CPMG) spin-echo pulse sequences were used to compensate for the inhomogeneity of the polarizing magnetic field. To generate versatile pulse sequences while using minimal electronic parts, we devised a new circuit schematic for NMR electronics that has served as a blueprint for subsequent NMR systems.

9.5.2 Optimal NMR Probe Design

Reducing sample volume requirements can lead to the effective increase of cell concentrations. However, it can also lead to degradation of the signal-to-noise ratio (SNR), as the absolute level of the NMR signal is proportional to the sample volume. System miniaturization thus should be accompanied by measures to maintain or enhance SNR to truly improve the detection sensitivity. In the second generation of μNMR system, we focused on improving SNR by engineering the NMR probes.

The SNR of a NMR probe can be expressed as

$$SNR = \kappa M_0 \cdot \sqrt{\frac{\mu_0 Q \omega_0 V_c}{4 k_B T \Delta f}}, \tag{9.3}$$

where κ is the fraction of the coil volume (V_c) occupied by the samples (filling factor), M_0 is the nuclear magnetization of the sample, μ_0 is the vacuum permeability, ω_0 is the Larmor frequency, Q is the quality factor of an NMR coil, and Δf is the bandwidth of a receiver electronics. For a given NMR setup (i.e., the same magnets and electronics), SNR could be improved by increasing κ and Q, which are properties of the NMR probes. Indeed, we have demonstrated a new probe design that achieves both maximal $\kappa(\approx 1)$ and high Q ($\sim$25) [28]. In this design, the probe consisted of a solenoidal microcoil embedded in a microfluidic structure (Fig. 9.7a). Solenoidal coils were chosen for their higher SNR than planar or birdcage coils [53]. To increase κ, we adopted the cast-molding technique in device fabrication. First, the coils were wound around polyethylene tubes and subsequently immersed into a polymer (PDMS). After PDMS cure, the tubes were withdrawn to open up the fluidic channels. With this design, the entire bore of the coil was available for samples; in one example, the new probe displayed >350 % larger SNR than a similar coil wrapped around a tube (Fig. 9.7b). Compared to the lithographically patterned planar coils in our previous systems [22], the improvement in SNR was much more significant (>20-fold enhancements); the solenoidal coil excited larger volumes of

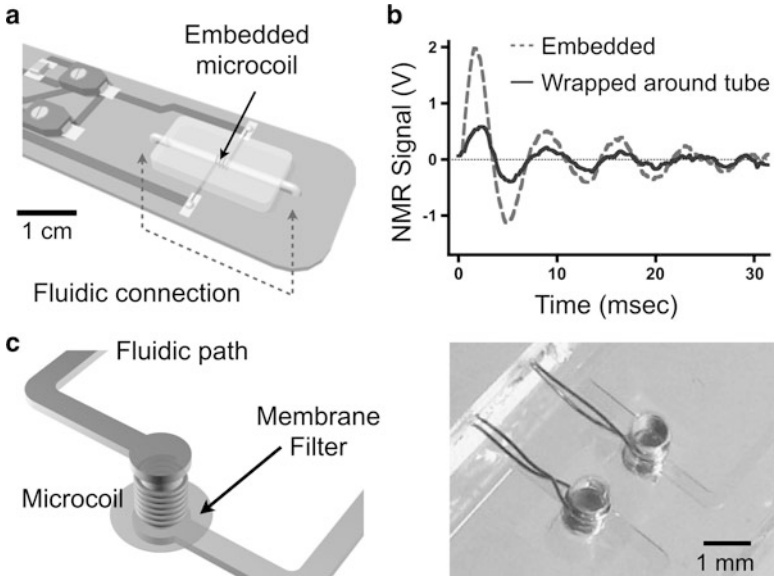

Fig. 9.7 *New NMR coils for higher sensitivity*. (**a**) A solenoidal coil is embedded along with a microfluidic channel. The entire bore of the coil is available to samples, maximizing the filling factor ($\approx$1). (**b**) The new coil, due to its high filling factor, offered >350 % enhancement in SNR compared to a similar coil wrapped around a tubing. (**c**) The R_2 changes can be amplified by concentrating MNP-labeled samples inside the microcoil. Based on the coil design in (**a**), we incorporated a filter that captures target objects. The photo shows a prototype device containing 100-nm pore filter (Adopted from [28] and [25]. Copyright 2009 National Academy of Sciences, USA and John Wiley and Sons, Inc.)

samples by producing more homogeneous radio-frequency magnetic fields and had smaller electrical resistance (e.g., 0.3 vs. 3.2Ω at 20 MHz).

We have further modified the embedded coil to improve the overall SNR and to streamline the assay procedure. In the new probe design, a cell-capturing membrane filter was incorporated at the outlet side of the coil (Fig. 9.7c). The filter serves two essential functions. First, it size selectively captures cells and concentrates them inside the NMR detection coil, which leads to more pronounced R_2 changes (Eq. 9.2). The filter also provides a way to detect a small number of targets from large sample volumes. Second, the filter enables on-chip separation of cells from unbound MNPs, therefore obviating the need for separate off-chip purification steps (e.g., centrifugation). Together with the highly magnetic Fe@ferrite MNPs, this new probe has been applied to diagnose tuberculosis [25]. Using the attenuated *bacillus Calmette-Guérin* (BCG) as a surrogate for *Mycobacterium tuberculosis*, we detected as few as 20 colony-forming units (CFUs) in sputum (1 mL). Importantly, the entire detection procedure was performed in a single-chip format, minimizing sample loss and making the assay simple and fast (in less than 30 min).

9.5.3 Clinical System

Our third-generation μNMR system is designed for practical applications in a clinical environment (Fig. 9.8) [57]. Its small size, easy accessibility, and high robustness provide end users with fast and stable measurements of biological samples. The new μNMR system is composed of three core parts: a newly designed probe for clinical samples, NMR electronics, and a user-friendly software.

The system design is based on that of previous generations of μNMR and consists of a small portable magnet ($B_0 = 0.5$ T) and a solenoidal coil for higher SNR (Fig. 9.8 *left*). A custom-made PMMA (polymethyl methacrylate) housing cages the magnet, the microcoil, and RF matching circuit. With its major improvement focused on clinical translatability, this new system uses disposable thin-walled polyimide tubes to load biological samples for measurement, thereby eliminating potential contamination of the NMR probe. The disposable tubes are filled with samples (~5 μL) and are inserted into the coil bore for NMR detection. Modular coils made in a variety of sizes can be plugged into the system to optimally accommodate available sample volumes (1–100 μL).

A small form-factor (20 × 12 × 5 cm) NMR electronics is implemented using off-the-shelf integrated circuit (IC) chips to achieve cost-effective (<$200) and highly programmable NMR platform (Fig. 9.8 *middle*). The NMR electronics generates the NMR pulse sequences, acquires the NMR signal, and communicates with external terminals (computer, mobile devices). It has three main parts: a microcontroller unit (MCU), an RF transmitter, and a signal receiver. The MCU (TMS320F28235, Texas Instruments) controls overall RF transceiver operations as well as data communication with external terminals. As an RF transmitter, a direct digital synthesis chip (AD9954, Analog Devices) is employed to generate two RF signals with 90° phase difference that are modulated by voltage-controlled switches (ADG1419BRMZ, Analog Devices). The RF heterodyne system is implemented to process the NMR signal. First, the signal is amplified by low-noise amplifier (AD604, Analog Devices) and down-converted to baseband (1–10 kHz) by a mixer (ADE-6, Mini-Circuits). Baseband signals subsequently pass a low-pass filter and are digitized by an analog-to-digital converter (AD7625, Analog Devices). Mobile devices (e.g., iPhone™, iPad™), which are connected to the MCU via a standard communication channel (e.g., USB, Bluetooth), receive digital data and show graphical outputs.

The NMR software incorporates graphical user interface (GUI), data acquisition/process, data logging/sharing, and a temperature compensation engine, which deliver a user-friendly interface and contribute to the robustness of the new μNMR system (Fig. 9.8 *right*). The software is programmed with Objective-C using Cocoa and Cocoa Touch frameworks and operates on iOS™ and OS X™. In order to implement a graphical representation of R_2 relaxation curve, open-source plotting framework (Core Plot) is cross-linked with Cocoa and Cocoa Touch frameworks. Time domain NMR data are acquired at the negative edge of spin echoes and processed real time. Negative edge-triggered data acquisition reduces the size of

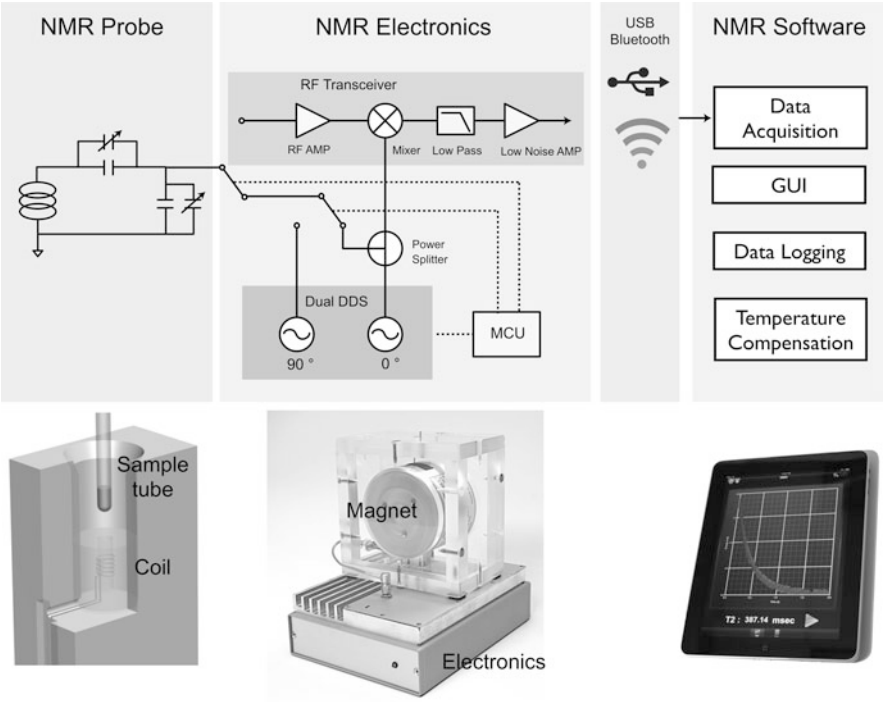

Fig. 9.8 *Overview of the clinical μNMR system*. The entire system was redesigned for robust operation in clinics. The NMR probe accepts samples sealed in disposable tubes to prevent probe contamination (*left*). NMR coils are embedded into the polymer support to open up the entire coil bore, and a thin-walled (thickness ∼65 μm) tube is used to minimize loss in filling factor. Block diagram of the NMR electronics for sample excitation and NMR signal reception (*middle*). The electronics is highly programmable and can be controlled via external terminals. Functional view of NMR software that processes data and shows graphical output of NMR measurements (*right*)

the data to be transferred and consequently decreases the data acquisition time via USB/Bluetooth connections by more than 10-fold. Transferred NMR data are then processed to obtain T_2 relaxation time. The overall signal pattern is displayed, and the data is stored in the terminal device. In addition, wireless communication module is embedded in the software for data logging/sharing over an encrypted wireless network, promoting usability in a remote clinical site.

To ensure stable and reliable T_2 relaxation time measurements, a temperature compensation engine has been implemented to run independently from the main thread. This temperature compensation engine transforms NMR data from time domain to frequency domain using fast Fourier transformation (FFT) and detects any changes in the NMR frequency due to environmental temperature fluctuation (described below).

9.5.3.1 Temperature Compensation

The NMR frequency f_0 is the parameter that requires most frequent adjustments and affects the measured NMR signals most significantly. The frequency f_0 changes as the magnetic field (B_0) from the permanent magnet drifts with temperature [58]. For example, with a 1°C increase in temperature, B_0 field from a NdFeB magnet will drop ~0.1 % from its initial value, and f_0 will proportionally decrease by 0.1 %; when the initial f_0 is 20 MHz ($B = 0.47$ T), the frequency change is then ~20 kHz. Such changes can place down-converted NMR signals near or beyond the low-frequency cutoff in the amplification stage, distorting the measured signal. Commercial benchtop NMR systems address the problem by housing the entire magnet block inside a heated container. This solution, however, significantly undermines the portability of the system due to the use of bulky and power-consuming parts. In the new μNMR system, we employed a dynamic control approach. Namely, programmable hardware in the NMR electronics and temperature compensation engine in the NMR software are designed to track and compensate for temperature dependency of the system. These implementations ensure optimal measurement settings for reliable and robust performance.

Figure 9.9a and b show the algorithm for temperature compensation. The feedback loop tracks the Larmor frequency f_0 and reconfigures the frequency f of NMR excitation. Coarse-tuning mode starts with initial NMR excitation frequency f_i and increases f by Δf. When the spectral power (P) of NMR spin echo reaches a predefined threshold P_{th}, a fine-tuning mode takes over to measure the frequency offset $f_d (= |f - f_0|)$. The fine tuning iterates until f_d reaches a target value. The target f_d value is carefully selected to keep down-converted NMR signal within the passband of the low-pass filter. Once the new NMR excitation frequency f has been established, CPMG pulse sequence is used to measure the T_2 relaxation time of the sample.

Figure 9.9c demonstrates the effectiveness of the developed temperature compensation method. When f_0 was allowed to drift but the RF frequency (f) for sample excitation was fixed, T_2 values varied up to 200 % relative to its starting value with typical fluctuation of room temperature ($\Delta T \sim 2$°C). When the temperature compensation engine was activated, however, T_2 variations were significantly reduced to <1 %. We further tested the system in environmental settings with a wide range of temperature differences (4–50°C). To determine the measurement accuracy, the linear dependence of T_2 on temperature was utilized. Figure 9.9d shows the T_2 values of an MNP solution monitored at different temperature. For a given environment setting, the μNMR system was operated with the temperature tracking activated to compensate for minute temperature variations (~1°C). The results show a linear relationship ($R^2 > 98$ %) as theoretically predicted, demonstrating the capacity for reliable T_2 measurements in various settings.

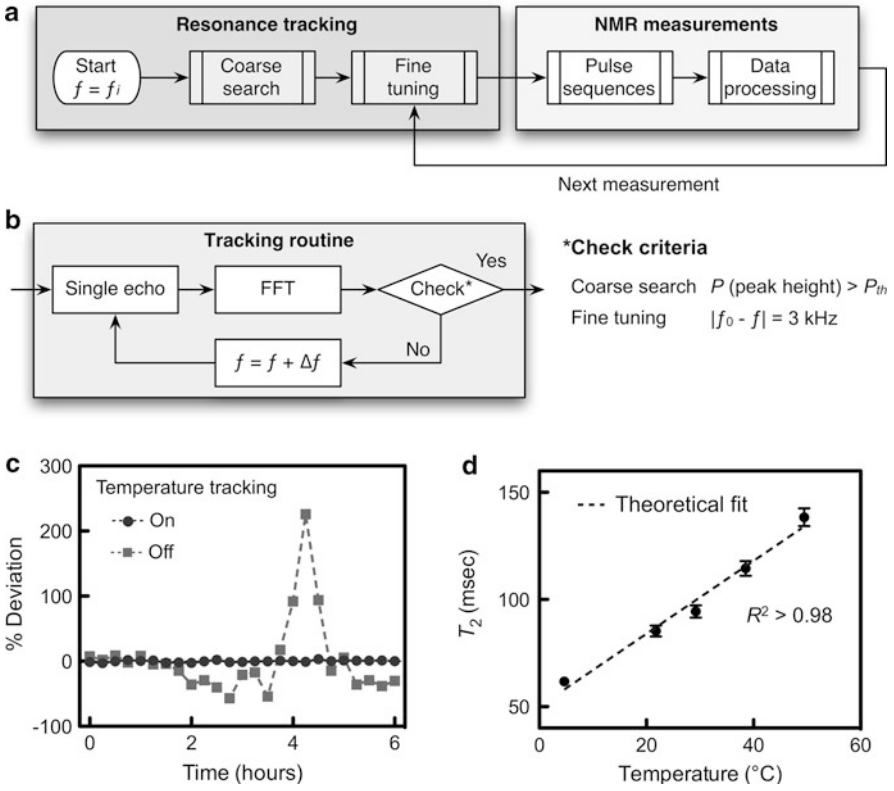

Fig. 9.9 *Automated temperature tracking in the new portable μNMR system*. (**a**) A flow diagram of the temperature compensation engine. The tracking routine searches for the Larmor frequency f_0 at a given environmental setting, using the successive tracking routines (coarse and fine). Once f_0 is determined, a full NMR measurement is performed. (**b**) Temperature tracking algorithm. For a given RF excitation with the frequency f, a spin echo signal is measured and transformed into the frequency domain via fast Fourier transform (FFT). The coarse search mode checks whether the amplitude (P) of a peak in the spectral power is larger than the predefined value (P_{TH}). In the next stage, the fine search mode iteratively tunes f until the frequency offset $f_d (= |f - f_0|)$ reaches the optimal offset value (~3 kHz). (**c**) The effectiveness of temperature compensation was evaluated using an MNP solution ($T_2 \approx 100$ ms). When the tracking routine was turned off (*square*), the T_2 variation was >200 % of its initial value. With the tracking routine turned on (*circle*), the fluctuation was significantly reduced (<1 %). (**d**) The robustness of μNMR measurements across a broad range of temperature (4–50°C) was demonstrated. The *dotted line* indicates a theoretical prediction (Reproduced from [57]. Copyright 2011 RSC Publishing)

9.6 Biological Applications

9.6.1 Cancer Detection and Profiling

Sensitive detection and rapid characterization of tumor cells in minimally processed biological samples will have significant impact on both biomedical research and clinical practice. Using the first-generation DMR device (μNMR-1) [22], DMR

molecular profiling of cancer markers (Her2/*neu*, EGFR, and EpCAM) on human cells was demonstrated with CLIO nanoparticles directly conjugated to monoclonal antibodies. With the development of the second-generation μNMR-2 and the highly magnetic $MnFe_2O_4$ nanoparticles, subsequent cellular detection sensitivity was remarkably improved to approximately single-cell level, far surpassing the sensitivity of other conventional clinical methods (Fig. 9.10a). Furthermore, a new assay protocol was established that reports the expression level of a specific biomarker and the target cell density.

To independently measure cell numbers by μNMR, we exploited a phenomenon of low-grade phagocytosis of nontargeted MNPs by tumor cells [59]. When mammalian cells were incubated (15 min at 37°C) with unmodified MNPs (MNP-Φ), linear and cell-number-dependent R_2 changes (ΔR_2^{Φ}) were observed (Fig. 9.10b). Interestingly, these changes were similar across a wide variety of cell types. The results were fitted to Eq. 9.2; $\Delta R_2^{\Phi} = r_2^{\Phi} \cdot n_C$, where r_2^{Φ} is the cellular relaxivity for MNP-Φ and n_C is the cell concentration (N_C / V). The cellular relaxivities (r_2^{Φ}) were statistically identical ($p > 0.99$) among different tumor cell lines, suggesting that the method may provide a universal measure for estimating n_C.

Using Eq. 9.2 and the cell density information (above), the expression level (ξ) of a select marker was defined as

$$\xi^{Ab} = \frac{\Delta R_2^{Ab}}{\Delta R_2^{\Phi}} = \frac{r_2^{Ab} \cdot n_C}{r_2^{\Phi} \cdot n_C} = \frac{r_2^{Ab}}{r_2^{\Phi}}, \tag{9.4}$$

where ΔR_2^{Ab} and r_2^{Ab} are R_2 changes and the cellular relaxivity, respectively, with a marker-specific MNP. In this normalized form, ξ now reports the *cellular* expression level of a targeted marker, providing a way to molecularly profile target cells regardless of cell numbers in a sample. The method was extensively verified by comparing μNMR measurements to other standard methods (flow cytometry, Western blotting) [22, 27, 28]. In one set of experiments, we measured the expression level of HER2 in breast cancer cell lines (Fig. 9.10c). The measured ξ^{HER2} ($= \Delta R_2^{HER2} / \Delta R_2^{\Phi}$) from μNMR (requiring $\sim 10^3$ cells) showed good agreement ($R^2 > 98\,\%$) with both flow cytometry (requiring $\sim 10^5$ cells) and Western blotting (requiring $\sim 10^7$ cells), validating the analytical capability of DMR. Note that DMR detection was much faster ($\sim$15 min) and performed using $> 10^2$ times fewer cells.

9.6.2 Clinical Trial

Through the integration of the complementary DMR and BOND technologies, this chip-based NMR detection platform has been applied in clinical trials of cancer cell profiling [26]. A total of 50 patients with suspected abdominal malignancies were enrolled. Each patient underwent fine-needle aspiration (FNA) using a 22-G needle, followed by routine core biopsies (17-G needle) for conventional analysis. The FNA samples were aliquoted and profiled for 11 predefined cellular markers:

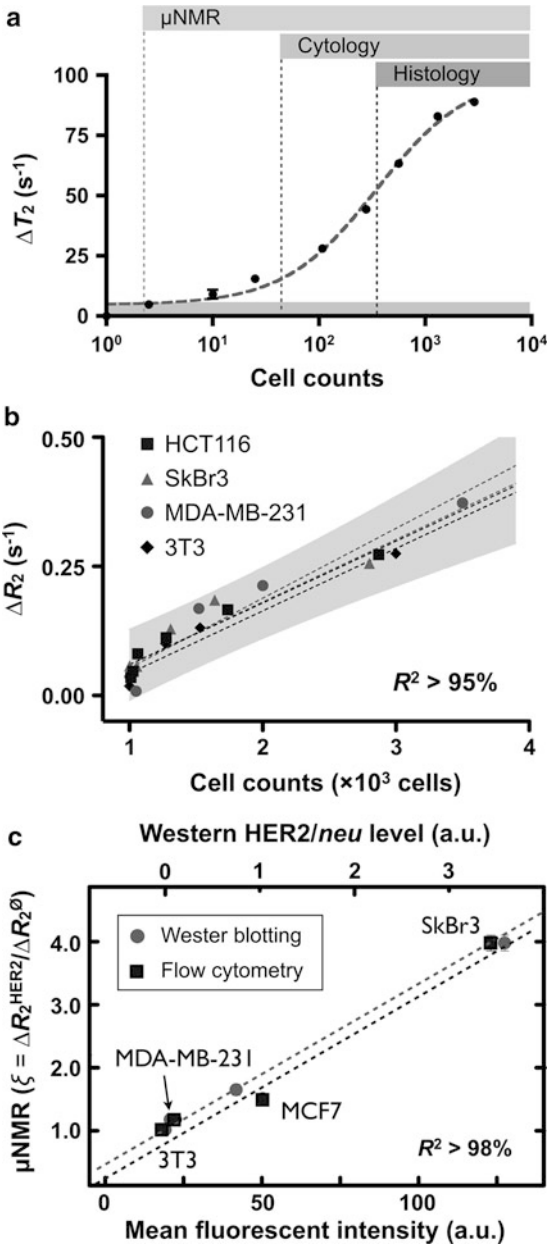

Fig. 9.10 *Cellular detection via DMR*. (**a**) The detection limit by DMR is nearly at single cell level (∼2 cells), which is superior to the current clinical methods (cytology and histology). (**b**) The uptake of unmodified MNPs by cells was exploited to estimate the cell population in the samples. The measured ΔR_2 was linearly proportional to the cell concentrations. Importantly, the linear trends were statistically identical in different cell types. (**c**) The analytical accuracy of the μNMR was benchmarked against flow cytometry and Western blotting by measuring HER2/*neu* expression on breast cancer cells (Adopted from [28]. Copyright 2009 National Academy of Sciences, USA)

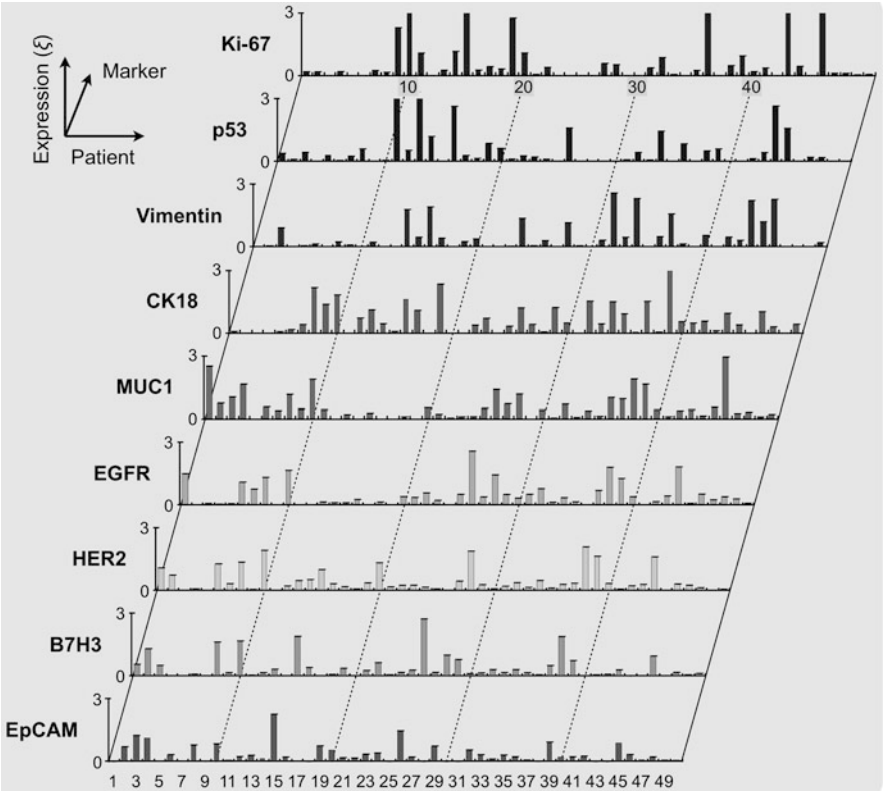

Fig. 9.11 *Expression levels of different biomarkers arranged by patient number*. Note the high degree of heterogeneity of marker expression per person. Patients 5, 12, 17, 18, 21, and 42 had benign lesions. x-axis, patient number; y-axis, expression level (ξ) of a marker (Reproduced from [26]. Copyright 2011 American Association for the Advancement of Science AAAS)

9 cancer-related markers (EpCAM, MUC-1, HER2, EGFR, B7H3, CK18, Ki-67, p53, Vimentin), CD45 for leukocyte counts, and control (MNP-Φ) to measure the total cell density. A priori selection of cancer markers was based on current practice (e.g., EpCAM, CK18) [60, 61] or on reports of clinically relevant overexpression [62–64]. On average, 3,850 cells were obtained per patient via FNA. Of these, approximately one-third were CD45-positive leukocytes (mean: 1,273 cells), and the remaining were nonleukocytic, primarily tumor cells as determined by flow cytometry. The aliquots (containing $\sim$350 cells) were labeled using the BOND method and measured by the clinical μNMR system. The R_2 data with CD45 was used to account for the contribution by leukocytes; for each cancer marker, its *cellular expression level* (ξ) was obtained based on Eq. 9.3.

Figure 9.11 shows the profiling results of 9 cancer markers for 50 patients. When plotted for each patient, the expression level of the markers showed considerable

Table 9.2 Sensitivity, specificity, and accuracy with DMR

Number	Marker	ξ value*	Sensitivity (%)	Specificity (%)	Accuracy (%)
Single	MUC1	0.25	66	83	68
	EGFR	0.20	64	83	66
	B7H3	0.11	68	67	68
	HER2	0.24	64	100	68
	Ki-67	0.10	68	67	68
	EpCAM	0.21	59	67	60
	Vimentin	0.08	59	67	60
	CK18	0.06	73	50	70
	p53	0.38	41	83	46
Dual	EpCam + CK18 (unweighted)	0.27	84	50	80
Triple	MUC1 + HER2 + EGFR (weighted)	1.23	95	67	92
Quad	MUC1 + HER2 + EGFR + EpCAM (weighted)	1.60	100	67	96

*Cutoff ξ value for identification of malignancy. The value was determined from the point on a receiver operating characteristic curve that has the minimal distance between the 0 % false negative and the 100 % true positive

heterogeneity across samples, which reconfirmed the importance of multiple-marker screening in cancer detection. Indeed, when analyzed for the diagnostic sensitivity, specificity, and accuracy (Table 9.2), a single marker showed accuracy of <70 %. The highest accuracy for cancer diagnosis with our cohort was obtained with a quadruple marker combination (MUC1 + EGFR + HER2 + EpCAM, 96 % accuracy), followed closely by weighted triple markers (MUC1 + EGFR + HER2, 92 % accuracy). Interestingly, the EpCAM and CK18 combination, which is routinely used in detecting circulating tumor cells in peripheral blood, achieved an overall diagnostic accuracy of 80 %, wherein high sensitivity (84 %) was offset by low specificity (50 %).

The DMR results were also compared to those by standard-of-care methods. Conventional cytology on FNA specimen was performed in 49 of 50 cases and was diagnostic in 36 cases with 11 misdiagnoses (accuracy 74 %). Conventional histology on all 50 biopsy samples correctly diagnosed 37 cases out of 45 diagnostic samples (accuracy 84 %), with the remaining results nondiagnostic (5 cases). DMR consistently outperformed the other methods, with 2 misdiagnoses in all 50 samples (accuracy up to 96 %). Also note that DMR permitted fast detection (in less than 60 min for each patient), whereas the mean clinical turnaround time (from sample submission to final report) was 3 days for cytology (1–8 days) and 4 days for surgical pathology (1–11 days).

9.7 Conclusions and Outlook

As a novel biosensing platform, DMR offers many synergistic advantages over traditional approaches, such as high detection sensitivity, multiplexed capability, rapid measurement, and small sample volume requirement with minimal sample processing. Indeed, DMR thrives through the complement of several cutting-edge technologies, namely, magnetic nanomaterials, bioconjugation chemistry, and microfabrication. With new developments such as chip-based μNMR devices, optimized magnetic nanoparticles, and advanced labeling techniques, the DMR technology has proven itself as a robust and sensitive approach for quantitative and molecular analyses for biomedical research. Moreover, our recent clinical trial has confirmed that the DMR is capable of detecting and molecularly profiling cells with minimal false negatives. Its remarkable performance and potential impact on clinical disease management would no doubt accelerate the advance of personalized treatment by providing valuable information on molecular signature of individual patients.

We further envision broader application of the DMR in global healthcare. The DMR technology does not require extensive sample purification and can be packaged as a portable device. The system thus is well suited for rapid and point-of-care (POC) testing, especially in resource-limited primary clinics where majority of diagnoses are made based on physical symptoms only. Indeed, we plan to evaluate the developed system for TB (tuberculosis) detection in fields. Successful completion of this research will be a cornerstone for realizing POC technology for TB detection, which will bring significant societal benefits worldwide.

Acknowledgements We thank T. J. Yoon, J. H. Chung, J. B. Haun, and N. Sergeyev for assistance with experiments and R. M. Westervelt (Harvard) and C. Castro (MGH) for many helpful discussions. This work was supported in part by the following NIH grants: U54CA151884, R01EB010011, R01EB004626, P01CA069246, P50CA86355, U01CA141556, U24CA092782, and R21CA14122. H. Shao acknowledges financial support from the B.S.-Ph.D. National Science Scholarship awarded by the Agency for Science, Technology and Research, Singapore.

References

1. R. Etzioni et al., The case for early detection. Nat. Rev. Cancer **3**, 243–252 (2003)
2. R. Fan et al., Integrated barcode chips for rapid, multiplexed analysis of proteins in microliter quantities of blood. Nat. Biotechnol. **26**, 1373–1378 (2008)
3. D.A. Giljohann, and C.A. Mirkin, Drivers of biodiagnostic development. Nature **462**, 461–464 (2009)
4. M.M. Cheng et al., Nanotechnologies for biomolecular detection and medical diagnostics. Curr. Opin. Chem. Biol. **10**, 11–19 (2006)
5. A.G. Tibbe et al., Optical tracking and detection of immunomagnetically selected and aligned cells. Nat. Biotechnol. **17**, 1210–1213 (1999) 1999.
6. M.M. Wang et al., Microfluidic sorting of mammalian cells by optical force switching. Nat. Biotechnol. **23**, 83–87 (2005)

7. E. Stern et al., Label-free immunodetection with CMOS-compatible semiconducting nanowires. Nature **445**, 519–522 (2007)
8. G. Zheng et al., Multiplexed electrical detection of cancer markers with nanowire sensor arrays. Nat. Biotechnol. **23**, 1294–1301 (2005)
9. S.C. Bendall et al., Single-cell mass cytometry of differential immune and drug responses across a human hematopoietic continuum. Science **332**, 687–696 (2011)
10. J. Cheon, and J.H. Lee, Synergistically integrated nanoparticles as multimodal probes for nanobiotechnology. Acc. Chem. Res. **41**, 1630–1640 (2008)
11. N.A. Frey et al., Magnetic nanoparticles: synthesis, functionalization, and applications in bioimaging and magnetic energy storage. Chem. Soc. Rev. **38**, 2532–2542 (2009)
12. Y.W. Jun, J.W. Seo, and J. Cheon, Nanoscaling laws of magnetic nanoparticles and their applicabilities in biomedical sciences. Acc. Chem. Res. **41**, 179–189 (2008)
13. Q.A. Pankhurst et al., Applications of magnetic nanoparticles in biomedicine. J. Phys. D: Appl. Phys. **36**, 167–181 (2003)
14. Y.R. Chemla et al., Ultrasensitive magnetic biosensor for homogeneous immunoassay. Proc. Natl. Acad. Sci. U.S.A. **97**, 14268–14272 (2000)
15. R.L. Millen et al., Giant magenetoresistive sensors. 2. Detection of biorecognition events at self-referencing and magnetically tagged arrays. Anal. Chem. **80**, 7940–7946 (2008)
16. V. Schaller et al., Towards an electrowetting-based digital microfluidic platform for magnetic immunoassays. Lab Chip **9**, 3433–3436 (2009)
17. D.R. Baselt et al., A biosensor based on magnetoresistance technology. Biosens. Bioelectron. **13**, 731–739 (1998)
18. R.S. Gaster et al., Matrix-insensitive protein assays push the limits of biosensors in medicine. Nat. Med. **15**, 1327–1332 (2009)
19. R.L. Millen et al., Giant magnetoresistive sensors and superparamagnetic nanoparticles: a chip-scale detection strategy for immunosorbent assays. Anal. Chem. **77**, 6581–6587 (2005)
20. S.J. Osterfeld et al., Multiplex protein assays based on real-time magnetic nanotag sensing. Proc. Natl. Acad. Sci. U.S.A. **105**, 20637–20640 (2008)
21. T. Aytur et al., A novel magnetic bead bioassay platform using a microchip-based sensor for infectious disease diagnosis. J. Immunol. Methods **314**, 21–29 (2006)
22. H. Lee et al., Chip-NMR biosensor for detection and molecular analysis of cells. Nat. Med. **14**, 869–874 (2008)
23. M. Gueron, Nuclear-relaxation in macromolecules by paramagnetic-ions – novel mechanism. J. Magn. Reson. **19**, 58–66 (1975)
24. J.M. Perez et al., DNA-based magnetic nanoparticle assembly acts as a magnetic relaxation nanoswitch allowing screening of DNA-cleaving agents. J. Am. Chem. Soc. **124**, 2856–2857 (2002)
25. H. Lee, T.J. Yoon, and R. Weissleder, Ultrasensitive detection of bacteria using core-shell nanoparticles and an NMR-filter system. Angew. Chem. Int. Ed Engl. **48**, 5657–5660 (2009)
26. J.B. Haun et al., Micro-NMR for rapid molecular analysis of human tumor samples. Sci. Transl. Med. **3**, 71ra16 (2011)
27. J.B. Haun et al., Bioorthogonal chemistry amplifies nanoparticle binding and enhances the sensitivity of cell detection. Nat. Nanotechnol. **5**, 660–665 (2010)
28. H. Lee et al., Rapid detection and profiling of cancer cells in fine-needle aspirates. Proc. Natl. Acad. Sci. U.S.A. **106**, 12459–12464 (2009)
29. M. Liong et al., Multiplexed magnetic labeling amplification using oligonucleotide hybridization. Adv. Mater. **23**, H254–H257 (2011)
30. P. Gillis, and S.H. Koenig, Transverse relaxation of solvent protons induced by magnetized spheres: application to ferritin, erythrocytes, and magnetite. Magn. Reson. Med. **5**, 323–345 (1987)
31. Y. Gossuin et al., Magnetic resonance relaxation properties of superparamagnetic particles. Wiley Interdiscip. Rev. Nanomed. Nanobiotechnol. **1**, 299–310 (2009)
32. R.A. Brooks, F. Moiny, and P. Gillis, On T2-shortening by weakly magnetized particles: the chemical exchange model. Magn. Reson. Med. **45**, 1014–1020 (2001)

33. P. Gillis, F. Moiny, and R.A. Brooks, On T(2)-shortening by strongly magnetized spheres: a partial refocusing model. Magn. Reson. Med. **47**, 257–263 (2002)
34. C. Massin et al., High-Q factor RF planar microcoils for micro-scale NMR spectroscopy. Sens. Actuat. A **97–98**, 280–288 (2002)
35. R.A. Brooks, T(2)-shortening by strongly magnetized spheres: a chemical exchange model. Magn. Reson. Med. **47**, 388–391 (2002)
36. J.M. Perez et al., Magnetic relaxation switches capable of sensing molecular interactions. Nat. Biotechnol. **20**, 816–820 (2002)
37. L. Josephson et al., High-efficiency intracellular magnetic labeling with novel superparamagnetic-Tat peptide conjugates. Bioconjug. Chem. **10**, 186–191 (1999)
38. J.H. Lee et al., Artificially engineered magnetic nanoparticles for ultra-sensitive molecular imaging. Nat. Med. **13**, 95–99 (2007)
39. S. Sun et al., Monodisperse MFe2O4 (M = Fe, Co, Mn) nanoparticles. J. Am. Chem. Soc. **126**, 273–279 (2004)
40. Y.W. Jun et al., Nanoscale size effect of magnetic nanocrystals and their utilization for cancer diagnosis via magnetic resonance imaging. J. Am. Chem. Soc. **127**, 5732–5733 (2005)
41. S. Peng et al., Synthesis and stabilization of monodisperse Fe nanoparticles. J. Am. Chem. Soc. **128**, 10676–10677 (2006)
42. T.J. Yoon et al., Highly magnetic core-shell nanoparticles with a unique magnetization mechanism. Angew. Chem. Int. Ed Engl. **50**, 4663–4666 (2011)
43. J. Park et al., Ultra-large-scale syntheses of monodisperse nanocrystals. Nat. Mater. **3**, 891–895 (2004)
44. Z. Chen et al., Preparation and characterization of water-soluble monodisperse magnetic iron oxide nanoparticles via surface double-exchange with DMSA. Colloid. Surf. A **316**, 210–216 (2008)
45. N. Fauconnier et al., Thiolation of maghemite nanoparticles by dimercaptosuccinic acid. J. Colloid Interface Sci. **194**, 427–433 (1997)
46. M. Liong et al., Carboxymethylated polyvinyl alcohol stabilizes doped ferrofluids for biological applications. Adv. Mater. **22**, 5168–5172 (2010)
47. J. Panyam, and V. Labhasetwar, Biodegradable nanoparticles for drug and gene delivery to cells and tissue. Adv. Drug Deliv. Rev. **55**, 329–347 (2003)
48. N.A. Peppas, and R.E.J. Benner, Proposed method of intracordal injection and gelation of poly (vinyl alcohol) solution in vocal cords: polymer considerations. Biomaterials **1**, 158–162 (1980)
49. K.M. Rosenblatt, and H. Bunjes, Poly(vinyl alcohol) as emulsifier stabilizes solid triglyceride drug carrier nanoparticles in the alpha-modification. Mol. Pharm. **6**, 105–120 (2009)
50. N.K. Devaraj et al., Fast and sensitive pretargeted labeling of cancer cells through a tetrazine/trans-cyclooctene cycloaddition. Angew. Chem. Int. Ed Engl. **48**, 7013–7016 (2009)
51. M.R. Karver, R. Weissleder, and S.A. Hilderbrand, Synthesis and evaluation of a series of 1,2,4,5-tetrazines for bioorthogonal conjugation. Bioconjug. Chem. **16**, 2263–2270 (2011)
52. S.S. Agasti et al., Supramolecular host-guest interaction for labeling and detection of cellular biomarkers. Angew Chem Int Ed Engl **51**, 450–454 (2012)
53. A.G. Webb, Radiofrequency microcoils in magnetic resonance. Prog. Nucl. Magn. Reson. Spectrosc. **31**, 1–42 (1997)
54. J. Grimm et al., Novel nanosensors for rapid analysis of telomerase activity. Cancer Res. **64**, 639–643 (2004)
55. C. Kaittanis, S.A. Naser, and J.M. Perez, One-step, nanoparticle-mediated bacterial detection with magnetic relaxation. Nano Lett. **7**, 380–383 (2007)
56. J.M. Perez, L. Josephson, and R. Weissleder, Use of magnetic nanoparticles as nanosensors to probe for molecular interactions. Chembiochem **5**, 261–264 (2004)
57. D. Issadore et al., Miniature magnetic resonance system for point-of-care diagnostics. Lab Chip **11**, 2282–2287 (2011)
58. E. Danieli et al., Small magnets for portable NMR spectrometers. Angew. Chem. Int. Ed Engl. **49**, 4133–4135 (2010)

59. A. Moore, R. Weissleder, and A.J. Bogdanov, Uptake of dextran-coated monocrystalline iron oxides in tumor cells and macrophages. J. Magn. Reson. Imaging **7**, 1140–1145 (1997)
60. S. Nagrath et al., Isolation of rare circulating tumour cells in cancer patients by microchip technology. Nature **450**, 1235–1239 (2007)
61. L.V. Sequist et al., The CTC-chip: an exciting new tool to detect circulating tumor cells in lung cancer patients. J. Thorac. Oncol. **4**, 281–283 (2009)
62. S.B. Ho et al., Heterogeneity of mucin gene expression in normal and neoplastic tissues. Cancer Res. **53**, 641–651 (1993)
63. T.J. Roth et al., B7-H3 ligand expression by prostate cancer: a novel marker of prognosis and potential target for therapy. Cancer Res. **67**, 7893–7900 (2007)
64. C.L. Vogel et al., Efficacy and safety of trastuzumab as a single agent in first-line treatment of HER2-overexpressing metastatic breast cancer. J. Clin. Oncol. **20**, 719–726 (2002)